Emergence, Coalescence, and Topological Properties of Multiple Exceptional Points and Their Experimental Realization

Kun Ding, Guancong Ma, Meng Xiao, Z. Q. Zhang, and C. T. Chan*

Department of Physics and Institute for Advanced Study, Hong Kong University of Science and Technology, Clear Water Bay, Kowloon, Hong Kong

(Received 31 December 2015; revised manuscript received 5 March 2016; published 12 April 2016)

Non-Hermitian systems distinguish themselves from Hermitian systems by exhibiting a phase transition point called an exceptional point (EP), at which two eigenstates coalesce under a system parameter variation. Many interesting EP phenomena, such as level crossings in nuclear and condensed matter physics, and unusual phenomena in optics, such as loss-induced lasing and unidirectional transmission, can be understood by considering a simple 2×2 non-Hermitian matrix. At a higher dimension, more complex EP physics not found in two-state systems arises. We consider the emergence and interaction of multiple EPs in a four-state system theoretically and realize the system experimentally using four coupled acoustic cavities with asymmetric losses. We find that multiple EPs can emerge, and as the system parameters vary, these EPs can collide and merge, leading to higher-order singularities and topological characteristics much richer than those seen in two-state systems. The new physics obtained is not limited to the acoustic systems demonstrated here. It also applies to other systems as well, such as coupled photonic cavities and waveguides.

DOI: 10.1103/PhysRevX.6.021007 Subject Areas: Acoustics, Materials Science

I. INTRODUCTION

Non-Hermitian systems [1–3] such as open and/or lossy systems are ubiquitous in nature. Systems with parity-time (PT) symmetry [4], as a subset of non-Hermitian systems, have generated great interest recently due to a rich array of novel phenomena including a divergent Petermann factor [5,6], loss-induced revival of lasing [7], single-mode lasers [8,9], reversed pump dependence of lasers [10], Bloch oscillation [11], coherent absorption [12], optical isolation [13], unidirectional light propagation [14–16], and others [17–23]. Many of these novel phenomena can be traced to the existence of an "exceptional point" (EP) when two quasibound states coalesce, which is perhaps the single most important characteristic of non-Hermitian physics. The EP can be described locally by a nondiagonalizable 2×2 matrix in which the eigenvalues have a square-root singularity and the eigenstates exhibit peculiar topological properties [24,25]. Recently, exceptional points have also been reported in some quantum systems such as Bose-Einstein condensates trapped in a PT-symmetric double-well potential [26,27] and nontopological superconductors [28]. Periodic systems can support more complex phenomena such as a ring of EPs, but even these complex configurations can still be considered using a 2×2 matrix [29]. However, for multistate systems, the interesting physics arising from non-Hermiticity is not limited to those EPs that can be described by a 2×2 matrix. For example, the PT symmetry recovery behaviors have been found in multiple optical waveguide system [30,31] and photonic crystals [32]. In general, multiple EPs can form [32–36] in a multistate system, and their interactions may lead to the coalescence of two or more EPs, which in turn gives rise to new physics including new singularities with different topological properties, which cannot be described by a 2×2 matrix [32–36].

In this work, we investigate a four-state system both theoretically and experimentally. The emergence of multiple EPs, their topological properties, and their coalescence can be best summarized in a phase diagram featuring an exceptional point formation pattern (EPFP). The coalescence of two EPs and that of three EPs forms two curves in the parameter space, partitioning the phase space into three regions each with a unique EPFP. Together with a two-state inversion line, the phase space is further divided into five regions, each with distinct topological properties. By using coupled acoustic resonant cavities with tunable eigenfrequencies, coupling strengths, and dissipative loss, these EPFPs were observed experimentally. The coalescence of three EPs produces a higher-order singularity, and the coalescence of a pair of EPs with the same chirality produces a linear crossing that is qualitatively different from the linear crossing at a diabolic point of Hermitian Hamiltonians [37]. It is worth mentioning that the acoustic system with multiple EPs considered here can be used for

*Corresponding author.
phchan@ust.hk

mode selection, similar to the modal demultiplexing found in PT-symmetric multiple optical waveguides [31], which, in fact, are also ideal optical platforms to realize the physical phenomena found in our work.

II. TWO COUPLED ACOUSTIC CAVITY RESONATORS

We begin with a two-state system containing two coupled cavities A and B having the same resonant frequency ω_2 as shown in the inset of Fig. 1(a). The Hamiltonian of the system can be written as

$$H = \begin{pmatrix} \omega_2 - i\Gamma_0 & \kappa \\ \kappa & \omega_2 - i\Gamma \end{pmatrix}, \tag{1}$$

where κ denotes the strength of the coupling, Γ_0 denotes the intrinsic loss of each cavity, and $\Gamma = \Gamma_0 + \Delta\Gamma$, with $\Delta\Gamma$ representing an additional tunable loss introduced at cavity B. The eigenfrequencies of Eq. (1) take the form

$$\tilde{\omega}_{1,2} = \omega_2 - i\frac{\Gamma + \Gamma_0}{2} \pm \frac{1}{2}\sqrt{4\kappa^2 - (\Delta\Gamma)^2}. \tag{2}$$

When $\Delta\Gamma$ is increased and becomes $2|\kappa|$, this two-cavity system will exhibit an EP at the square-root branch point. At this point, the two eigenstates coalesce and one becomes defective. Beyond this point, the imaginary part of the frequency (the "width") of the two states bifurcates.

The above Hamiltonian [Eq. (1)] can be realized with acoustic resonant cavities, as shown in Fig. 1(a). We begin by studying the behavior of a single acoustic cavity. We fabricate cylindrical metallic (stainless-steel) cavities by precision machining. The cavity's fundamental mode has an eigenfrequency ω_2, which can be tuned by varying its depth h through the relation $\omega_2 = \pi v/h$, where v is the speed of sound in air. All the cavities have the same radius of 15.0 mm. The cavities are filled with air at one atmospheric pressure, with temperature kept at 295 K. Small ports of 2.5 mm in diameter are opened on the top of the cavities for external pumping, which also introduce radiation loss that contributes to Γ_0. Microphones (PCB Piezotronics Model-378C10) are inserted into the sidewalls of the cavities near the bottom for pressure measurement. Lock-in amplifiers (Stanford Research SR-830) are used to drive a loudspeaker, as well as to record the signals from the microphones. The measured pressure of a single acoustic cavity with $h = 50.6$ mm is shown by red open squares in Fig. 1(b), which clearly shows the resonant peak. The resonant frequency ω_2 and intrinsic loss Γ_0 of the single cavity can be obtained by fitting the measured spectrum of pressure amplitude according to $|P(\omega)| \propto |\{1/[\omega - (\omega_2 - i\Gamma_0)]\}|$ after a steady-state excitation, and the fitting results are shown by the red line in Fig. 1(b). Experimentally, the main source of uncertainty is due to the temperature fluctuation of air. We carefully monitor the temperature and are able to maintain the fluctuation within ± 0.5 K. The temperature uncertainty propagates to an uncertainty that is no larger than ± 0.6 Hz in the cavity's resonance peaks (see Supplemental Material, Sec. VII, for detailed analysis of experimental uncertainties [38]). The size of the symbols for the experimental data points already takes into account the measurement uncertainties.

To introduce additional loss, we insert small pieces of sponge into the top or bottom of a cavity symmetrically. However, these sponges slightly redshift the resonant frequency. To compensate for this shift, we further add a

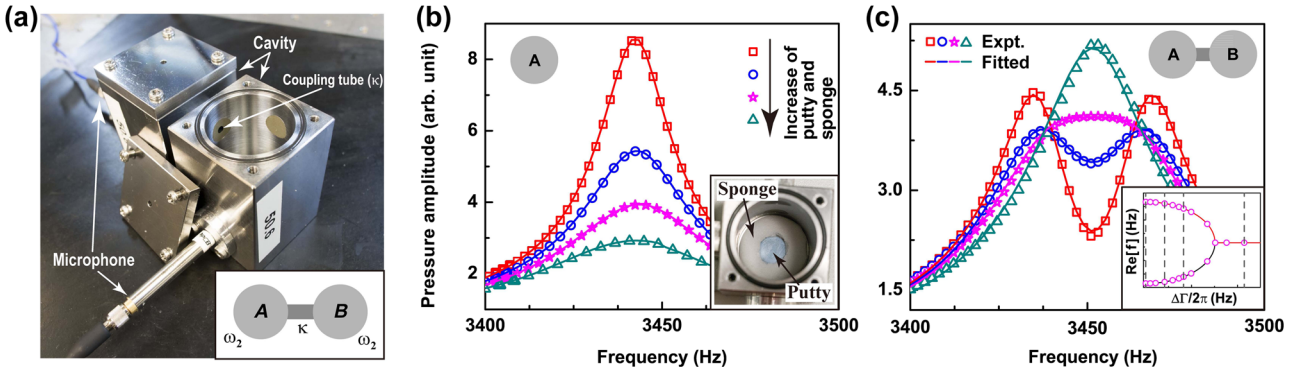

FIG. 1. (a) A photograph of two acoustic cavity resonators (labeled A and B in the inset) coupled by side tubes. Cavity B is opened and disconnected to show its interior and the coupling tubes. The inset is a schematic picture of the system. (b) Measured pressure responses as functions of frequency (symbols) of a single cavity ($h = 50.6$ mm) with increasing loss. The inset in (b) shows the arrangement of sponge and putty which is stuck to the bottom of the metallic cavity, and the amount of them is controlled by their mass. (c) Measured pressure response spectra (symbols) of the two coupled cavities. Cavities A and B have the same depth, $h = 50.6$ mm. Coupling κ is achieved using two side tubes with radii of 2.0 and 0.8 mm, respectively. Asymmetric loss is introduced in cavity B, whereas both pumping and measurements are performed at cavity A. Solid curves in (b) and (c) are numerical fittings using a Green function method [Eq. (3)]. The inset in (c) shows fitted results of real parts of eigenfrequencies as a function of asymmetric loss $\Delta\Gamma$. The vertical dashed lines in the inset correspond to the four $\Delta\Gamma$ shown in (c). The formation of an exceptional point at which the two states coalesce can be clearly seen.

small amount of Blu-Tack putty, which decreases the volume and consequently blueshifts the resonant frequency. Therefore, the assembly of sponge and putty as shown in the inset of Fig. 1(b) yields a total effect that ideally reproduces $\Delta\Gamma$, as shown by blue, magenta, and dark cyan symbols in Fig. 1(b) for different amounts of the assembly in the single cavity. To determine the value of $\Delta\Gamma$, we again fit $|P(\omega)|$ to the Lorentz pole with Γ_0 replaced by $\Gamma_0 + \Delta\Gamma$, as shown by the solid lines in Fig. 1(b). The good agreement with experimental results and fitted ones clearly demonstrates that this metallic acoustic cavity with additional assembly of sponge and putty could realize the desired on-site resonant state in the Hamiltonian.

We could use two connected acoustics cavities to achieve experimental realization of the Hamiltonian Eq. (1), as shown in Fig. 1(a). A set of small tubes having the same length of 15.0 mm but various radii are also machined out of stainless steel. Side ports in the cavity are fabricated to accommodate coupling tubes. The couplings can be adjusted by choosing the tube's cross-sectional area. For this configuration, we choose two side tubes with radii of 2.0 and 0.8 mm, respectively, to produce the coupling κ. The open symbols in Fig. 1(c) show the measured pressure responses at cavity A (with pumping also at cavity A) for increasing additional loss at cavity B.

To retrieve the eigenmodes from these experimental data, we build the Green function of our system with N states by using the eigenvalues and right or left eigenvectors of the Hamiltonian as

$$\overleftrightarrow{G}(\omega) = \sum_{j=1}^{N} \frac{|\tilde{\phi}_j^R\rangle\langle\tilde{\phi}_j^L|}{\omega - \tilde{\omega}_j}, \tag{3}$$

where $|\tilde{\phi}_j^R\rangle$ and $\langle\tilde{\phi}_j^L|$ are the normalized biorthogonal right and left eigenvectors, and $\tilde{\omega}_j$ are eigenvalues (see also Supplemental Material, Sec. I [38]). It should be pointed out that Eq. (3) has higher-order terms when the system is exactly at the EP [39], but experimentally we can never be exactly at the EP, so all the higher-order terms are ignored in this method. Then the analytical response function is $|P(\omega)| = A|\langle p|\overleftrightarrow{G}(\omega)|s\rangle|$, where $|s\rangle$ and $|p\rangle$ are two column vectors describing the source and probe information. For example, in this two-cavity case [$N = 2$, cavities A and B in Fig. 1(a)] the two basis vectors are $(1,0)^T$ for A and $(0,1)^T$ for B.

The first step in the fitting process is to obtain the values of the system parameters ω_2, Γ_0, and κ in the Hamiltonian. In the fitting process, the system parameters are iteratively improved until the difference of the calculated pressure function $|P(\omega)|$ calculated according to Eq. (3) and the measured pressure response data for the sample without the putty and sponge [red squares in Fig. 1(c)] are minimized in the least-square sense. A convergent and good fitting implies that the two-level model captures the essence of the physics. The results fitted to the red squares in Fig. 1(c) are plotted by the red solid line, which indeed shows good agreement, indicating that our model is good enough to produce the experimental results. The second step of the fitting is to obtain the asymmetric loss parameter $\Delta\Gamma$ using the values of ω_2, Γ_0, and κ obtained in the first step. The procedure is similar to the previous step; namely, we do the least-square fitting of the measured pressure response with the putty and sponge included [blue circles, magenta stars, and cyan triangles in Fig. 1(c)] to the response function $|P(\omega)|$ of Eq. (3). The fitted results, represented by the blue, magenta, and cyan solid lines in Fig. 1(c), also agree well with the measured data, confirming the validity of our Green function method. In the inset of Fig. 1(c), we use the values of ω_2, Γ_0, and κ obtained in the first fitting step in Eq. (2) and plot the EPFP as a function of $\Delta\Gamma$ in solid curves. The fitted results of $\Delta\Gamma$ obtained in the second step for different amounts of sponge and putty are marked by dashed vertical lines in the inset. The intercepts of the solid curves and vertical lines denoted by circles indicate the eigenfrequencies of the different samples measured. Other circles in the inset are also obtained from the fittings using samples not included explicitly in Fig. 1(c). In other words, the evolution of eigenfrequencies versus $\Delta\Gamma$ is constrained on the mathematical curve shown in the inset of Fig. 1(c) by having set the first three parameters with an accurate fit. The fourth parameter, $\Delta\Gamma$, when adjusted for each experimental case, gives responses that fit with a comparable accuracy of the experimental ones. From this inset, we see clearly that two eigenmodes coalesce at an EP when $\Delta\Gamma = 2|\kappa|$. Hence, we experimentally demonstrate an acoustic realization of the physics of exceptional points.

III. FOUR-STATE NON-HERMITIAN HAMILTONIAN WITH COUPLING

Using the above two-state system as the building block, we now construct a four-state system as shown in the inset of Fig. 2(a). The system consists of two pairs of coupled cavities with the same values of κ, Γ_0, and Γ but different resonant frequencies. Cavities A and B form one pair with resonant frequency ω_2, and cavities C and D form another pair with resonant frequency ω_1. Coupling between these two pairs is introduced by connecting cavities A and D with a small tube and cavities B and C with another small tube, as shown in the inset of Fig. 2(a). The Hamiltonian of the system can be written as

$$H = \begin{pmatrix} \omega_2 - i\Gamma_0 & \kappa & 0 & t \\ \kappa & \omega_2 - i\Gamma & t & 0 \\ 0 & t & \omega_1 - i\Gamma_0 & \kappa \\ t & 0 & \kappa & \omega_1 - i\Gamma \end{pmatrix}, \tag{4}$$

where t denotes the strength of interpair coupling, and additional losses are introduced in cavity B and D. The eigenfrequencies of Eq. (4) take the following form (see Appendix A):

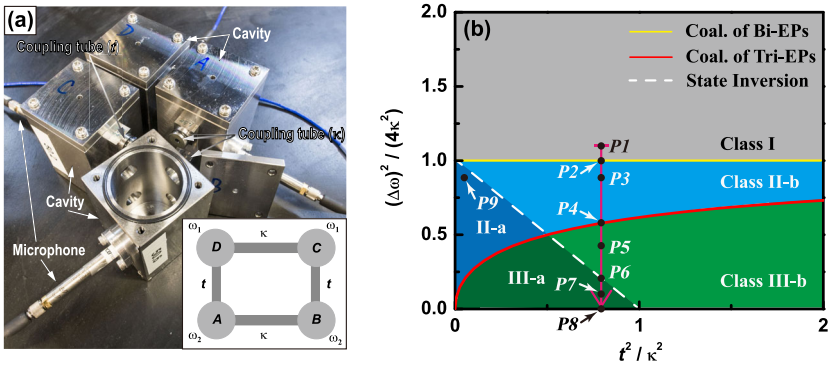

FIG. 2. (a) A photograph of four coupled acoustic cavity resonators (labeled $A-D$ in the inset, which shows a schematic drawing of the system). Here, A and B (C and D) form a pair with resonant frequency ω_2 (ω_1), with κ and t being the coupling between these resonators. Phase diagram in the $\Delta\omega \sim t$ space is shown in (b), with $\Delta\omega = \omega_1 - \omega_2$. In (b), the gray, blue, and green regions represent classes I, II, and III EPFPs, respectively. The solid red curve marks the coalescence of three EPs, the solid yellow line marks the coalescence of two EPs, and the white dashed line marks the state inversion line that separates subclasses "a" and "b" with different topological characteristics. The vertical red arrow line and the nine points (labeled from $P1$ to $P9$) are drawn to show the EPFP in Fig. 3.

$$\tilde{\omega}_j = \omega_0 - i\frac{\Gamma+\Gamma_0}{2} \pm \frac{1}{2}\sqrt{\Delta_1 \pm 4\sqrt{\Delta_2}}, \quad j = 1,2,3,4, \tag{5}$$

where $\omega_0 = (\omega_1 + \omega_2)/2$ and

$$\Delta_1 = -(\Delta\Gamma)^2 + 4\kappa^2 + 4t^2 + (\Delta\omega)^2, \tag{6}$$

$$\Delta_2 = 4\kappa^2 t^2 + \kappa^2(\Delta\omega)^2 - (\Delta\Gamma)^2\frac{(\Delta\omega)^2}{4}, \tag{7}$$

with $\Delta\omega = \omega_1 - \omega_2$. For the convenience of discussion, we put the four states in Eq. (5) in the following order: $j = 1:(-,+)$, $j = 2:(-,-)$, $j = 3:(+,-)$, and $j = 4:(+,+)$, where the first (second) sign in the brackets denotes the choice of the first (second) sign in Eq. (5) outside (inside) the first square root and $j = 1$ is the state with the lowest real frequency. Equation (5) shows that coalescence of states (CS) could occur under three conditions, which we refer to as CS-$1_\pm$: $\Delta_1 \pm 4\sqrt{\Delta_2} = 0$, $\Delta_2 \neq 0$, $\Delta_1 \neq 0$, CS-2: $\Delta_2 = 0$, $\Delta_1 \neq 0$, and CS-3: $\Delta_1 = \Delta_2 = 0$, respectively. CS-$1_\pm$ corresponds to a normal EP with one state defective. At CS-2, two different EPs occur simultaneously and each has one state defective. CS-3 corresponds to the coalescence of fours states with three states defective. We analyze the rich topological properties of these singularities later by examining the eigenvectors.

IV. EIGENFREQUENCY PHASE DIAGRAM AND EXPERIMENT REALIZATIONS

From Eqs. (6) and (7), we see that, depending on the parameters $(\Delta\omega)^2$, κ^2, and t^2, different combinations of CS-$1_\pm$, CS-2, and CS-3 may appear in the EPFP when $\Delta\Gamma$ is increased continuously. Figure 2(b) shows a phase diagram in the space of two dimensionless parameters $(\Delta\omega/2\kappa)^2$ and $(t/\kappa)^2$. Three regions exist, designated as classes I, II, and III, with their boundaries marked by a solid yellow line and a solid red line. Each class represents a distinct EPFP, in which the EPs can have different singularity types. In addition, class II and class III can each be further divided into two topologically distinct regions, designated a and b and separated by a white dashed line. We show later that while regions a and b share the same EPFP, they exhibit different topological characteristics.

To experimentally investigate the three classes of EPFP, we need a system to reproduce Eq. (4). To accomplish this, eight cavities with four different depths, 50.0, 50.2, 50.4, and 50.6 mm, are fabricated. The eigenfrequency can be further fine-tuned by adding a small amount of Blu-Tack putty inside the cavity, which slightly decreases the volume. Combining these two, we are able to cover the frequency range of $\Delta\omega$ experimentally. Two cavities with the same depth (and same amount of putty) are connected by the aforementioned side tubes to form a pair coupled by κ. Two different pairs are further connected together by another two small side tubes whose cross-sectional area determines the interpair coupling t. A photograph of the experimental realization is shown in Fig. 2(a).

A. Class I

To show the EPFP in each region, we choose a value of $(t/\kappa)^2 = 0.7744$ and then decrease $(\Delta\omega/2\kappa)^2$ continuously from 1.004 (point $P1$), as marked by the vertical red arrow line in Fig. 2(b). The point $P1$ lies in class I, which occupies the top area of the phase diagram. Here, owing to the large $\Delta\omega$, the two pairs of cavities are well separated in frequency and therefore can be regarded as nearly independent, even though coupling does exist. A typical EPFP is shown in Fig. 3(a). We find two CS-2 singularities in the spectrum; namely, one EP exists for each pair of the cavities.

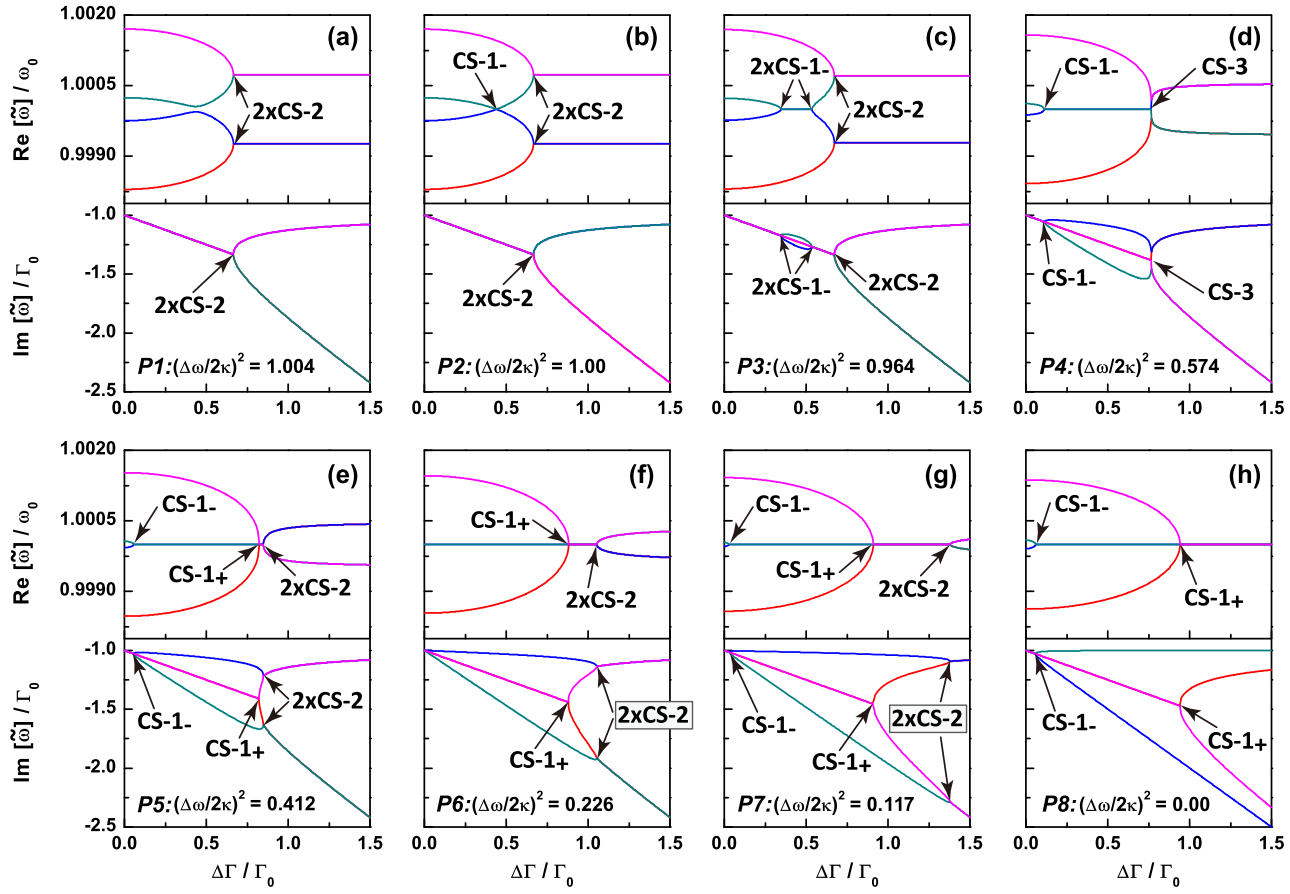

FIG. 3. Real and imaginary parts of eigenfrequencies as functions of asymmetric loss $\Delta\Gamma/\Gamma_0$ for points $P1$ to $P8$ in the phase diagram shown in Fig. 2(b) are plotted from (a) to (h) accordingly. The system parameters are $\omega_0 = 3427.59$ rad/s, $\kappa = -2.5$ rad/s, $t = -2.2$ rad/s, and $\Gamma_0 = 10$ rad/s. Each exceptional point is labeled to show its types according to the main text.

To realize class I by using acoustic cavity system, we choose $h = 50.6$ mm for cavities A and B, with 150 mg of putty inside, and the depth for cavities C and D is 50.0 mm. Intrapair coupling κ is provided by two side tubes with the same radius of 1.2 mm, connecting A to B and C to D. Two tubes with radius of 0.8 and 0.4 mm connect A to D and B to C to provide interpair coupling t. To excite all possible modes, measurements are performed 4 times with the loudspeaker driving each cavity individually. The arithmetic mean of these four results yields a spectrum under incoherent pumping. Additional loss $\Delta\Gamma$ is gradually increased only in cavities B and D by adding an assembly of sponge and putty. Microphones are used to measure the pressure at cavity B (filled symbols) and cavity D (open symbols). The measured results are shown in Fig. 4(a). It can be seen that initially there are two peaks in both cavity pairs (configuration M and N). As $\Delta\Gamma$ increases, the states belonging to the same pair of cavities coalesce (configuration O and P). This generates two EPs (at 3436.2 and 3471.0 Hz). Because of the large $\Delta\omega$, the two pairs are well separated in the frequency spectrum, so they may be considered as forming their own EPs nearly independently. To obtain the EPFP, similar to the case of two cavities, the first step is to obtain the values of the system parameters $\omega_{1,2}$, Γ_0, κ, and t. We fit the measured pressure response for the sample without sponge and putty [red squares in Fig. 4(a)] to the response function calculated by Eq. (3), from which we obtain the following system parameters: $(\Delta\omega/2\kappa)^2 = 3.665$ and $(t/\kappa)^2 = 0.094$, which lie in class I in the phase diagram shown in Fig. 2(b). In Fig. 4(b), we use these fitted values in Eq. (5) and plot the EPFP as a function of $\Delta\Gamma$ in solid curves. Then to identify the experimental asymmetric loss $\Delta\Gamma$ for each sample, similar to the second fitting step used in the two-cavity case, we fit the measured pressure response for the samples with the putty and sponge included [blue circles, magenta stars, and cyan triangles in Fig. 4(a)] to the response function calculated by Eq. (3). The agreement between measured data and Eq. (3) is still good, as shown by the blue, magenta, and cyan solid lines in Fig. 4(a). The fitted results of $\Delta\Gamma$ for different amounts of sponge and putty are marked by dashed vertical lines in Fig. 4(b). The intercepts of the solid curves and vertical lines denoted by circles indicate the eigenfrequencies of the different samples measured. Other circles in the inset are also obtained from the fittings using samples not included explicitly in Fig. 4(a). Two EPs

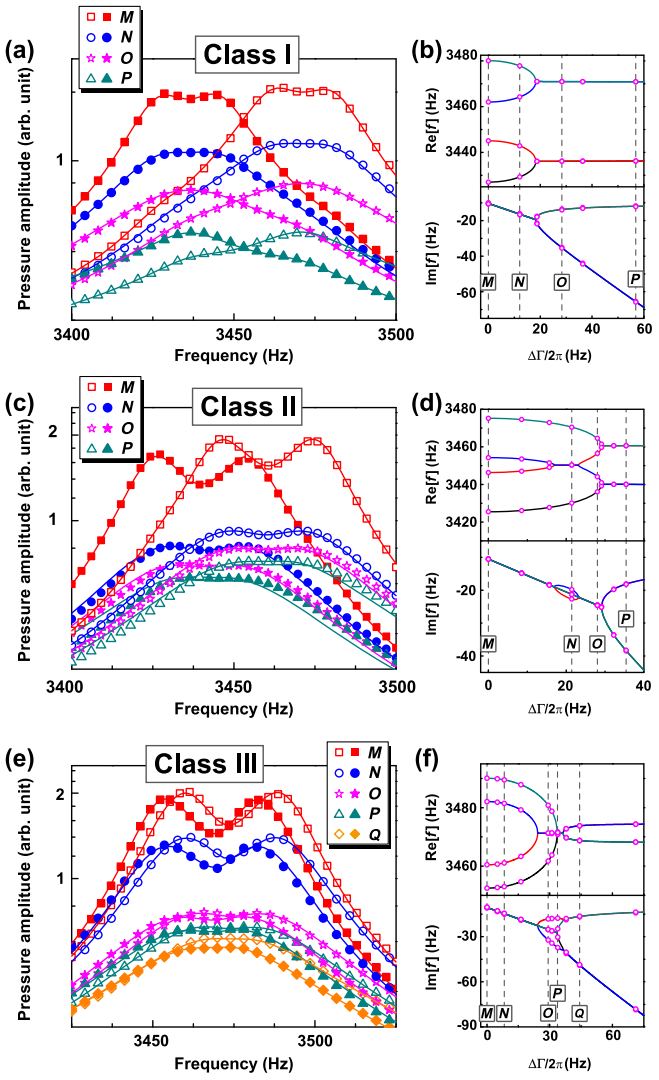

FIG. 4. Measured pressure response spectra at cavity B (filled symbols) and D (open symbols) for some certain point in class I (a), class II (c), and class III (e) separately. The coupled cavities are pumped incoherently. Results labeled M to P or Q show increasing amounts of asymmetric loss. The corresponding solid curves are fitted using a Green function method [Eq. (3)]. Real and imaginary parts of eigenfrequencies as functions of asymmetric loss $\Delta\Gamma$ for experimental results in (a), (c), and (e) are plotted in (b), (d), and (f) accordingly, in which open symbols are obtained by using parameters fitted from experimental results and solid lines are from analytical models by using fitted parameters without sponge and putty. The colors (black, red, blue, dark cyan) represent different eigenfrequencies of our model.

are clearly identified, a clear signature of a class-I EPFP [gray area in Fig. 2(b)].

B. Class II and coalescence of two EPs

Decreasing $(\Delta\omega/2\kappa)^2$ will bring the system to the yellow solid line in Fig. 2(b), which is given by $\alpha = [(\Delta\omega)^2/4\kappa^2] - 1 = 0$. This line separates class II from class I. When this line is approached from above (class I), the gap near $\Delta\Gamma/\Gamma_0 \cong 0.45$ in Fig. 3(a) will close when $\alpha = 0$, and the typical EPFP at $\alpha = 0$ (point $P2$) is shown in Fig. 3(b). It should be pointed out that the crossing point is linear, and theoretical proof is given in Appendix B (see also Supplemental Material, Sec. II [38]). Further decreasing $(\Delta\omega/2\kappa)^2$, this linear crossing point will split into two CS-1_ singularities, and this gives a typical EPFP of class II (point $P3$), as shown in Fig. 3(c). The two CS-1_-type singularities are given by the two roots of $F \equiv \Delta_1 - 4\sqrt{\Delta_2} = 0$. In other words, when the $\alpha = 0$ line is approached from below (class II), the two CS-1_ singularities coalesce to form a linear crossing. This line is obtained from two conditions: $F = \Delta_1 - 4\sqrt{\Delta_2} = 0$ and $[(\partial F)/\partial(\Delta\Gamma)] = 0$ (also see Appendix A). We emphasize here that one state is defective at the linear crossing point induced by the coalescence of two EPs of the same chirality, and, as such, this linear crossing point is different from the diabolic point in a Hermitian Hamiltonian [37]. We discuss this in the next section.

To experimentally demonstrate a class-II EPFP, we decrease the eigenfrequency difference $\Delta\omega$ by reducing the depth difference between interpair cavities: $h = 50.6$ mm for cavities A and B, $h = 50.2$ mm for cavities C and D. In addition, intrapair coupling κ is increased by using two side tubes 2.0 and 0.8 mm in their radii. Interpair coupling is provided by side tubes 0.4 mm in radii, and the smaller side tubes provide a smaller interpair coupling t compared with the coupling in the experimental setting shown in Fig. 4(a). By using the first fitting step described for class I, we obtain the system parameters $(\Delta\omega/2\kappa)^2 = 0.79$ and $(t/\kappa)^2 = 0.017$, which indicate that the system is in class II in the phase diagram shown in Fig. 2(b).

As shown in Fig. 4(c), we can observe four peaks when $\Delta\Gamma = 0$ (configuration M). Comparing these with configuration M in Fig. 4(a), we can see that the resonance frequency of the lower-frequency peak of cavity D (open squares) is lower in frequency than that of the higher-frequency peak of cavity B (filled squares). This order is opposite of that in Fig. 4(a), in which the resonance frequency of the lower-frequency peak of cavity D (open squares) is higher than that of the higher-frequency peak at cavity B (filled squares). Such a change of order occurs only for the two middle peaks, and we call such a switching "state inversion," which can also be seen in the eigenfrequency spectrum [blue and red curves in Fig. 4(d)]. We will explain the physical consequences of this inversion in detail in Secs. IV D and V. The increase in $\Delta\Gamma$ first brings these two middle states to coalescence, with an EP occurring and the system enters a regime with three different $\mathrm{Re}[f]$ (configuration N). The values of $\Delta\Gamma$ are also determined by the second fitting step described in Secs. II and IV A. However, further increases in $\Delta\Gamma$ cause the eigenfrequencies of the upper state [green curves in Fig. 4(d)] and lower state [black curves in Fig. 4(d)] to move towards the central coalesced state at 3450 Hz. Eventually, the intrapair

interaction t is strong enough to pull the central state apart. This gives rise to the second EP, and the system reverts to the previous configuration with four different Re$[f]$ (configuration O). If we focus on the evolution of the two middle states, it appears that these two states coalesce as $\Delta\Gamma$ increases but bifurcate again as $\Delta\Gamma$ increases further. This cannot occur in a 2×2 system, but is allowed in higher dimensions. Eventually, $\Delta\Gamma$ is sufficiently large for the intrapair states to coalesce. Two more EPs are generated, and the system reaches its terminal stage with states of two different Re$[f]$ (configuration P).

C. Class III and coalescence of three EPs

Upon a further decrease in $(\Delta\omega/2\kappa)^2$, the EPFP will transit from class II-b [point $P3$, Fig. 3(c)] to class III-b [point $P5$, Fig. 3(e)] as the system parameters cross the solid red line in Fig. 2(b), which has the form

$$(\Delta\omega)^2 = 2\sqrt{t^4+4\kappa^2t^2}-2t^2. \tag{8}$$

Equation (8) is obtained by eliminating $\Delta\Gamma$ in equations $\Delta_1=0$ and $\Delta_2=0$ [see Eqs. (6) and (7) and also Appendix A]. As shown in Fig. 3(d) (point $P4$), the configurations on this red line always carry a CS-3-type singularity for some particular values of $\Delta\Gamma$ and three states are defective at the CS-3 points (see also Supplemental Material, Sec. III [38]). Such a singularity is a higher-order EP [32,33]. The red solid line hence represents a line of high-order singularities. In addition to the CS-3 singularity, there exists another CS-1_- singularity at a smaller value of $\Delta\Gamma$. Above the red line (in the class-II region), the CS-3 singularity splits into three singularities: one CS-1_- on the left and two CS-2's on the right. Below this red line (in the class-III region), the CS-3 singularity also splits into three singularities, but in a different manner: one CS-1_+ on the left and two CS-2's on the right having the same Re$(\tilde{\omega}_j)$ but different Im$(\tilde{\omega}_j)$. A typical EPFP of class III is shown in Fig. 3(e) (point $P5$). Interestingly, the yellow and red solid lines converge in the limit of large t^2/κ^2, which can be seen from Eq. (8).

To experimentally demonstrate a class-III EPFP, we further decrease $\Delta\omega$ and modify κ, t. Experimental parameters used in Fig. 4(e) are as follows: The depth of cavities A and B is 50.2 mm with 150 mg of putty inside; the depth of cavities C and D is 50.0 mm; the two κ tubes have radii of 2.0 and 0.8 mm; the two t tubes have radii of 0.4 and 0.8 mm. These system parameters we obtain from the first fitting step are $(\Delta\omega/2\kappa)^2=0.048$ and $(t/\kappa)^2=0.025$, which belong to class III in the phase diagram shown in Fig. 2(b). The results of experiments and theoretical fittings are shown in Figs. 4(e) and 4(f) in a similar manner. The values of $\Delta\Gamma$ are also obtained from the second fitting step. Following the increase in $\Delta\Gamma$, at the beginning, the system behaves similarly to class II in the configuration with no additional loss: the number of peaks starts at four (configurations M and N), and then the two middle states coalesce producing the first EP, which indicates the system has entered a stage with three different Re$[f]$ (configuration O). Subsequently, the upper and lower two states also coalesce (the second EP). The system enters a regime with only one real frequency (configuration P). Eventually, with a sufficiently large $\Delta\Gamma$, the system generates another two EPs and reaches the final stage with states of two different Re$[f]$ (configuration Q).

D. State inversion line

When $(\Delta\omega/2\kappa)^2$ is further decreased, we cross the white dashed line expressed by $4\kappa^2=4t^2+(\Delta\omega)^2$, which corresponds to the degeneracy condition of the two middle states in the absence of $\Delta\Gamma$ (also see Appendix A). So this white dashed line is the state inversion line. When $(\Delta\omega/2\kappa)^2=0.226$ [point $P6$, Fig. 3(f)], the system configuration resides at the boundary of classes III-a and III-b, which is marked by the white dashed line as shown in Fig. 2(b). On this line, the first EP (CS-1_-) disappears. An EP of opposite chirality reemerges when $(\Delta\omega/2\kappa)^2$ is further decreased and the eigenfrequencies of the two middle states are inverted [point $P7$, Fig. 3(g)]. Although the EPFPs in Figs. 3(e) and 3(g) appear to be the same when the system parameters cross the white dashed line (and hence they are called class III-a and class III-b, respectively), they have different chiralities associated with the CS-1_- singularity, as we discuss in the next section.

When $(\Delta\omega/2\kappa)^2$ is decreased further and gradually approaches zero, the two CS-2 singularities in Fig. 3(g) will approach infinity as $\Delta\omega$ approaches zero. The value of $\Delta\Gamma_{\text{CS-2}}$ can be obtained from Eq. (7) (see Supplemental Material, Sec. IV [38]); i.e.,

$$\Delta\Gamma_{\text{CS-2}}^2 = 4\kappa^2\left(1+\frac{4t^2}{(\Delta\omega)^2}\right). \tag{9}$$

Equation (9) shows that $\Delta\Gamma_{\text{CS-2}}$ approaches infinity as $\Delta\omega$ approaches zero and appears at a larger $\Delta\Gamma_{\text{CS-2}}$ for a nonzero $\Delta\omega$. On the other side, these two CS-2 singularities gradually approach the CS-1_+ singularity as $(\Delta\omega/2\kappa)^2$ increases. At $(\Delta\omega/2\kappa)^2=0$ (point $P8$), two EPs (CS-1_- and CS-1_+ corresponding, respectively, to $\Delta_1-4\sqrt{\Delta_2}=0$ and $\Delta_1+4\sqrt{\Delta_2}=0$) form with increasing $\Delta\Gamma$, as shown in Fig. 3(h).

V. TOPOLOGICAL CHARACTERISTICS AROUND SINGULARITIES

It is well known that there is one defective state at the EP, so the chirality of EP could be defined analogous to the polarization of electromagnetic waves; for instance, the chirality of EP is "right" if the eigenvector is $(-i,1)/\sqrt{2}$ and "left" if the vector at EP is $(i,1)/\sqrt{2}$, because there is only one independent eigenvector at the EP. It is also well

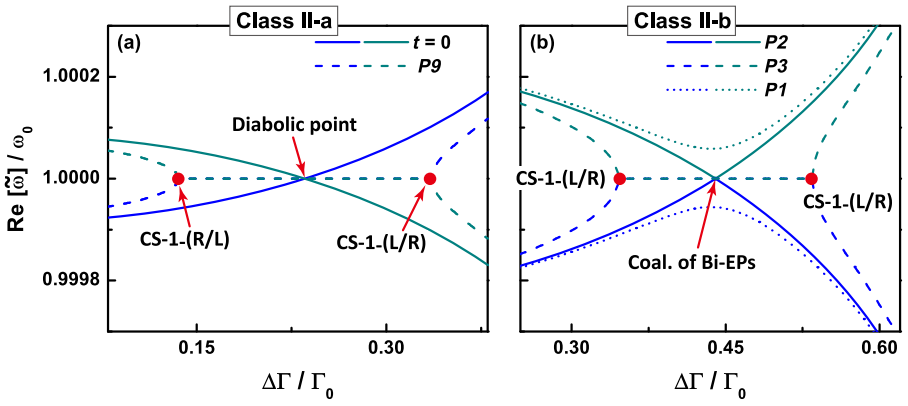

FIG. 5. Real parts of eigenfrequencies as functions of asymmetric loss for the point $P9$ in the phase diagram shown in Fig. 2(b) near the two CS-1_ are shown in (a) by dashed lines with system parameters $\omega_0 = 3427.59$ rad/s, $\kappa = -2.5$ rad/s, $t = -0.5$ rad/s, and $\Gamma_0 = 10$ rad/s. For comparison, the solid lines in (a) are for $t = 0$ rad/s while keeping all the other parameters the same with point $P9$. Real parts of eigenfrequencies as functions of asymmetric loss for the points $P1$, $P2$, and $P3$ in the phase diagram shown in Fig. 2(b) near the two CS-1_ are shown in (b) by dotted lines, solid lines, and dashed lines, respectively. The letters in the bracket following CS-1_ indicate the relative chirality of this EP.

known that a parameter variation encircling an EP will cause the two states to switch position after one cycle and acquire a geometric phase $\pm\pi$ after two cycles [24,25]. Thus, four cycles in parameter space are needed to restore the original eigenvectors. The origin of such behaviors comes from square-root singularity, as the singularity order is $1/2$. Here, we are particularly interested in both the topological difference between domains a and b in the phase diagram and topological characteristics of the singularities on the two solid lines in Fig. 2(b) on which two or three EPs coalesce.

To illustrate the difference between domains a and b in the phase diagram, we plot real parts of eigenfrequencies for point $P9$ and point $P3$ near the two CS-1_ singularities by dashed lines in Figs. 5(a) and 5(b), respectively. In Fig. 5(b), we also plot real parts of eigenfrequencies for point $P1$ and point $P2$ by dotted and solid lines. It has been stated before that the crossing of solid lines is linear.

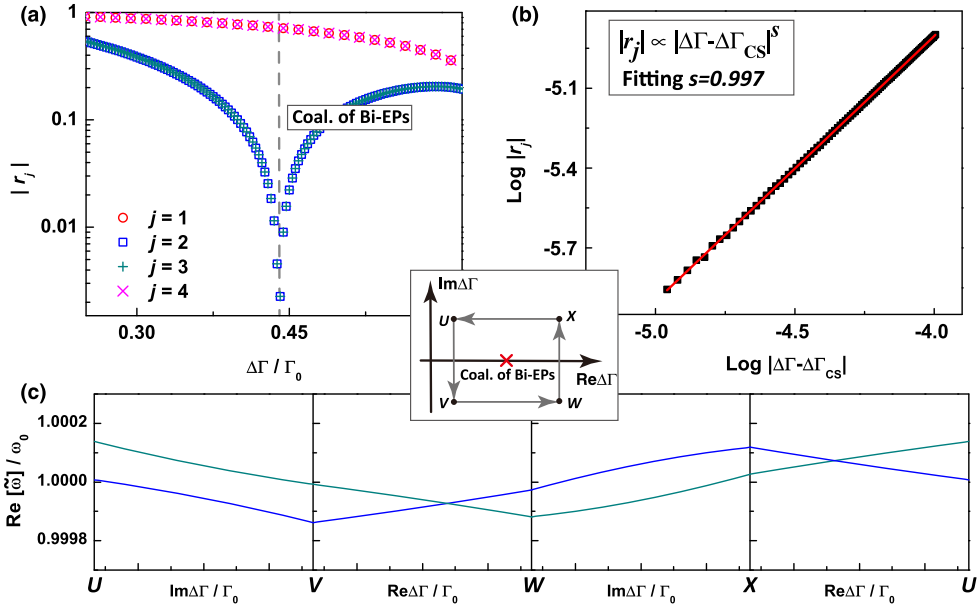

FIG. 6. (a) Phase rigidity of all the eigenstates as functions of asymmetric loss $\Delta\Gamma/\Gamma_0$ for the point $P2$ in the phase diagram shown in Fig. 2(b). (b) Log-log plot of phase rigidity $|r_j|$ versus $|\Delta\Gamma - \Delta\Gamma_{CS}|$ for the coalescence point of two CS-1_ singularities (filled squares). The fitting result is shown by the solid line, from which the exponent "s" of the power law is obtained. The inset shows the looping path in the complex-$\Delta\Gamma$ plane, in which the singularity locates inside the loop. (c) Eigenfrequency trajectories for looping around the coalescence point of two CS-1_ singularities in the counterclockwise direction ($U \to V \to W \to X \to U$) as shown in the inset.

For comparison, real parts of eigenfrequencies for the same parameters with point $P9$, except $t = 0$, are also shown in Fig. 5(a) by solid lines. The crossing of these solid lines is linear crossing, too (see Appendix C). So class II-a and class II-b share the same EPFP. But if we see the chirality of these EPs, domains a and b will be different. We can prove that the two CS-1_ singularities in Fig. 5(a) (class II-a) have opposite chirality (see Appendix C and Supplemental Material, Sec. V [38]). So these two EPs do cancel each other when they coalesce, producing a diabolic point [37]. Afterwards, no defective states exist at the coalescence point, which could be seen from theoretical results (see Appendix C). However, the first CS-1_ singularity in Fig. 5(a) changes chirality when the system passes through the state inversion line [white dashed line in Fig. 2(b)], namely transiting from point $P9$ to point $P3$ as shown in Fig. 5(b). Because of this change, the two CS-1_ singularities in Fig. 5(b) (class II-b) have the same chirality, so the coalescence of these two CS-1_ singularities could *not* cancel each other, but produces a higher-order singularity at the crossing point.

To identify the singularity order, we plot in Fig. 6(a) the absolute value of phase rigidity [2], defined as $r_j = \langle \tilde{\phi}_j^R | \tilde{\phi}_j^R \rangle^{-1}$ for each state j as a function of $\Delta\Gamma$ for the point $P2$ in the phase diagram. Phase rigidity is a measure of the mixing of different states. In the absence of $\Delta\Gamma$, all four states are distinct and their phase rigidity is close to unity. As $\Delta\Gamma$ is increased, phase rigidities are reduced as some states start to mix. Two states are completely mixed at the EP where the phase rigidity vanishes. It is clear that $|r_j|$ vanishes for states $j = 2$ and 3 at the linear crossing point at $\Delta\Gamma/\Gamma_0 \cong 0.45$, indicating a defective state. The log-log plot of $|r_j|$ shown by the red curve in Fig. 6(b) gives an exponent of 1. This is different from the exponent of $1/2$ for an ordinary EP, and is also different from a diabolic point in a Hermitian Hamiltonian where no singularity is found. Thus, the yellow line represents a line consisting of EPs with a singularity different from that of an isolated EP. To understand the exponent 1 physically, we have performed an adiabatic process encircling the singularity in the complex $\Delta\Gamma$ plane in a counterclockwise direction, as shown in the inset of Fig. 6. The imaginary part of $\Delta\Gamma$ represents a shift in the resonant frequency of the cavity. The trajectories of states 2 and 3 encircling the crossing point at $\Delta\Gamma/\Gamma_0 \cong 0.45$ are shown in Fig. 6(c), from which we find that only one cycle is required to bring the two states back to their original positions. The calculation of geometric phase by using the parallel transport method [40] gives a geometric phase of $\pm\pi$ after one cycle, consistent with the exponent of 1 found in Fig. 6(b). We have hence confirmed that the yellow solid line in the phase diagram is indeed a high-order singularity line.

To further identify the singularity order in the solid red line of the phase diagram, in Fig. 7(a), we plot the absolute value of phase rigidity of point $P4$ in the phase diagram. In CS-3 ($\Delta\Gamma/\Gamma_0 \cong 0.77$), all four states have zero rigidity, which indicates they are all linearly dependent with three defective states. In Fig. 7(b), we also plot $|r_j|$ as a function

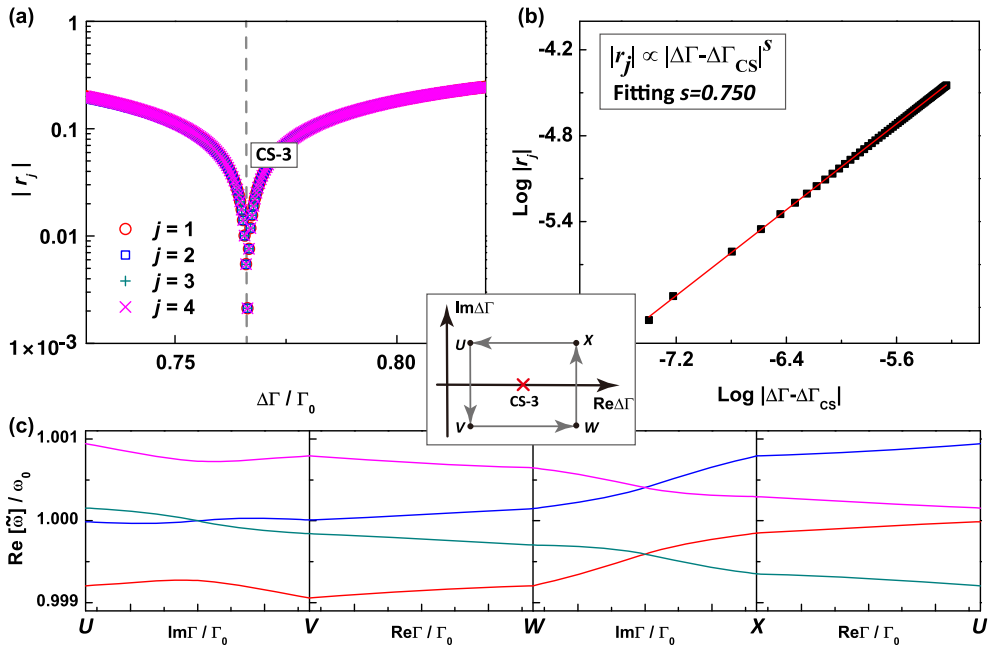

FIG. 7. (a) Phase rigidity of all the eigenstates as functions of asymmetric loss $\Delta\Gamma/\Gamma_0$ for the point $P4$ in the phase diagram shown in Fig. 2(b). (b) Log-log plot of phase rigidity $|r_j|$ versus $|\Delta\Gamma - \Delta\Gamma_{CS}|$ for the CS-3 singularities (filled squares), and the fitting result is shown by the solid line. The inset shows the looping path in the complex-$\Delta\Gamma$ plane, in which the CS-3 singularity locates inside the loop. (c) Eigenfrequency trajectories for looping around the CS-3 singularities in the counterclockwise direction ($U \to V \to W \to X \to U$) as shown in the inset.

of $|\Delta\Gamma - \Delta\Gamma_{\text{CS-3}}|$ in the log-log scale. A linear line with a slope of $3/4$ is found [32,33]. This corresponds to a higher-order singularity resulting from the coalescence of four states with three of them defective. To understand the exponent $3/4$ physically, we also perform an adiabatic process encircling the CS-3 singularity in the complex $\Delta\Gamma$ plane in a counterclockwise direction, as shown in the inset of Fig. 7. The trajectories of the four eigenfrequencies (real part) along the path are shown in Fig. 7(c), from which we see that it requires four cycles to bring an eigenstate back to its original position. We also calculate the geometric phase using the parallel transport method [40] and obtain a phase of $\pm 3\pi$ after four cycles. This indicates that eight cycles are required to restore the initial eigenvector.

Before concluding, we point out that the looping of singularities in the complex parameter plane can be considered as fractional winding numbers. For example, a winding number of $\pm 1/2$ means the geometric phase is $\pm\pi$ after 2 cycles around the singularity, and the sign $\pm$ is determined by the chirality of this EP. And then the cancellation of two EPs in Fig. 5(a) could be understood by $1/2 - 1/2 = 0$, and those in Fig. 5(b) are $1/2 + 1/2 = 1$. This highlights the difference between a and b in the phase diagram. To recap, we observe the higher-order wave function singularities of exponents 1 and $3/4$ due, respectively, to the coalescence of two EPs having the same chirality and the coalescence of three EPs.

VI. CONCLUSIONS

The experimental system, as shown in Fig. 2(a), can be viewed as a connected network of lossy cavities. The EP-related physics are expected to be even richer when the number of connected cavities is further increased where the symmetry of the network and the topology of the connectivity can serve as extra degrees of freedom. The new physics we obtain here should also apply to electromagnetic and matter waves. As singularities underlie the essence of EPs, the new singularities found in higher dimensions and their associated topological properties can serve as new platforms for realizing new phenomena.

ACKNOWLEDGMENTS

G. M. thanks Ping Sheng for helpful discussions and Zhiyu Yang for providing equipment and lab space. This work was supported by Research Grants Council, University Grants Committee, Hong Kong (Grant No. AoE/P-02/12).

K. D. and G. M. contributed equally to this work.

APPENDIX A: EIGENFREQUENCIES AND BOUNDARY LINES IN THE PHASE DIAGRAM

The Hamiltonian [Eq. (4)] used to describe an acoustic system composed of two pairs of acoustic cavities (for simplification, we assume $\omega_1 \geq \omega_2$) is

$$H = \begin{pmatrix} \omega_2 - i\Gamma_0 & \kappa & 0 & t \\ \kappa & \omega_2 - i\Gamma & t & 0 \\ 0 & t & \omega_1 - i\Gamma_0 & \kappa \\ t & 0 & \kappa & \omega_1 - i\Gamma \end{pmatrix} = H_0 + V, \tag{A1}$$

in which $\Delta\Gamma = \Gamma - \Gamma_0$,

$$H_0 = \begin{pmatrix} \omega_2 - i\Gamma_0 & \kappa & 0 & t \\ \kappa & \omega_2 - i\Gamma_0 & t & 0 \\ 0 & t & \omega_1 - i\Gamma_0 & \kappa \\ t & 0 & \kappa & \omega_1 - i\Gamma_0 \end{pmatrix}, \tag{A2}$$

$$V = \begin{pmatrix} 0 & 0 & 0 & 0 \\ 0 & -i\Delta\Gamma & 0 & 0 \\ 0 & 0 & 0 & 0 \\ 0 & 0 & 0 & -i\Delta\Gamma \end{pmatrix}. \tag{A3}$$

We note that the even mode has a lower frequency because of $\kappa < 0$ and $t < 0$. To see the physics, we could rotate H to the diagonal representation of H_0,

$$H = \left(\omega_0 - i\frac{\Gamma+\Gamma_0}{2}\right)\overleftrightarrow{I} + \begin{pmatrix} -|\kappa| - \frac{1}{2}\sqrt{\Theta} & -i\frac{\Delta\Gamma}{2}\frac{\Delta\omega}{\sqrt{\Theta}} & 0 & -i\Delta\Gamma\frac{|t|}{\sqrt{\Theta}} \\ -i\frac{\Delta\Gamma}{2}\frac{\Delta\omega}{\sqrt{\Theta}} & |\kappa| - \frac{1}{2}\sqrt{\Theta} & -i\Delta\Gamma\frac{|t|}{\sqrt{\Theta}} & 0 \\ 0 & -i\Delta\Gamma\frac{|t|}{\sqrt{\Theta}} & -|\kappa| + \frac{1}{2}\sqrt{\Theta} & i\frac{\Delta\Gamma}{2}\frac{\Delta\omega}{\sqrt{\Theta}} \\ -i\Delta\Gamma\frac{|t|}{\sqrt{\Theta}} & 0 & i\frac{\Delta\Gamma}{2}\frac{\Delta\omega}{\sqrt{\Theta}} & |\kappa| + \frac{1}{2}\sqrt{\Theta} \end{pmatrix}, \tag{A4}$$

in which $\omega_0 = (\omega_1 + \omega_2)/2$, $\Delta\omega = \omega_1 - \omega_2$, and $\Theta = 4t^2 + (\Delta\omega)^2$. Diagonalization of Eq. (A4) gives the eigenfrequencies as

$$\tilde{\omega}_j = \omega_0 - i\frac{\Gamma+\Gamma_0}{2} \pm \frac{1}{2}\sqrt{\Delta_1 \pm 4\sqrt{\Delta_2}}, \quad j = 1, 2, 3, 4, \tag{A5}$$

in which the order of eigenfrequencies follows as (in increasing values of real frequency) $j = 1:(-,+)$, $j = 2:(-,-)$, $j = 3:(+,-)$, $j = 4:(+,+)$, and two kernel elements are

$$\Delta_1 = -(\Delta\Gamma)^2 + 4\kappa^2 + 4t^2 + (\Delta\omega)^2, \tag{A6}$$

$$\Delta_2 = 4\kappa^2 t^2 + \kappa^2(\Delta\omega)^2 - (\Delta\Gamma)^2\frac{(\Delta\omega)^2}{4}. \tag{A7}$$

It is easy to see that what determine the properties of Eq. (A5) are intrapair loss difference $\Delta\Gamma$, intrapair coupling κ, interpair coupling t, and interpair frequency difference $\Delta\omega$.

For the special case with $\Delta\Gamma = 0$, the gap between state 2 and state 3 closes and reopens when $H_{22} = H_{33}$ in Eq. (A4), which defines this state inversion line, i.e.,

$$4\kappa^2 = 4t^2 + (\Delta\omega)^2. \tag{A8}$$

This is plotted by the white dashed line in Fig. 2(b).

As mentioned in the main text, Eq. (A5) gives four cases when coalescence of states (CS) can occur; i.e., (CS-1$_\pm$):$\Delta_1 \pm 4\sqrt{\Delta_2} = 0$, $\Delta_1 \neq 0$, $\Delta_2 \neq 0$, (CS-2): $\Delta_2 = 0$, $\Delta_1 \neq 0$, and (CS-3): $\Delta_1 = \Delta_2 = 0$. If we denote $F \equiv \Delta_1 - 4\sqrt{\Delta_2}$, the mathematical conditions under which the coalescence of two CS-1_ singularities could happen are $F = 0$ and $(\partial F/\partial\Delta\Gamma) = 0$; namely,

$$\begin{aligned} F &= \Delta_1 - 4\sqrt{\Delta_2} = 0, \\ \frac{\partial F}{\partial\Gamma} &= -2\Delta\Gamma\left[1 - \frac{(\Delta\omega)^2}{2\sqrt{\Delta_2}}\right] = 0. \end{aligned} \tag{A9}$$

Solving Eq. (A9) gives the following condition:

$$t^2[(\Delta\omega)^2 - 4\kappa^2] = 0 \Rightarrow t = 0 \quad \text{or} \quad (\Delta\omega)^2 = 4\kappa^2, \tag{A10}$$

which is plotted by a solid yellow line in Fig. 2(b).

Solving the CS-3 singularity condition $\Delta_1 = \Delta_2 = 0$ gives the following equations:

$$(\Delta\omega)^2 = 2\sqrt{t^4 + 4\kappa^2 t^2} - 2t^2, \tag{A11}$$

$$\Delta\Gamma^2 = 2|t|\sqrt{t^2 + 4\kappa^2} + 4\kappa^2 + 2t^2. \tag{A12}$$

If $|t| \to 0$, then $(\Delta\omega) = \sqrt{4|\kappa t|}$. And if $|t| \to \infty$, then $(\Delta\omega)^2 = 4\kappa^2$. Equation (A11) is plotted by a solid red line in Fig. 2(b).

APPENDIX B: LINEAR CROSSING AT THE COALESCENCE LINE OF TWO CS-1_ SINGULARITIES

In this case, we expand our system as

$$\frac{(\Delta\omega)^2}{4\kappa^2} = 1 + \alpha, \qquad |\alpha| \ll 1. \tag{B1}$$

When $\alpha = 0$, the eigenfrequencies of the system can be written as

$$\tilde{\omega}_j = \omega_0 - i\frac{\Gamma + \Gamma_0}{2} \pm \frac{1}{2}\left|2|\kappa| \pm \sqrt{4t^2 + 4\kappa^2 - (\Delta\Gamma)^2}\right|. \tag{B2}$$

It is not difficult to see that when $(\Delta\Gamma)^2 = 4t^2$, $\tilde{\omega}_2 = \tilde{\omega}_3$. If we do a small $\delta\Gamma$ expansion around the point $\Gamma_d = 2|t|$, i.e., $\Delta\Gamma = \Gamma_d + \delta\Gamma$, Eq. (B2) reduces to

$$\tilde{\omega}_{2,3} = \omega_0 - \frac{i}{2}(2\Gamma_0 + \Gamma_d + \delta\Gamma) \pm \frac{|t|}{2|\kappa|}\delta\Gamma, \tag{B3}$$

which indicates that there indeed exists a linear cross at Γ_d. If we do a small α expansion near $\alpha = 0$ while keeping $\delta\Gamma = 0$, Eq. (A5) gives

$$\tilde{\omega}_{2,3} = \omega_0 - i(\Gamma_0 + |t|) \pm |t|\sqrt{\alpha}. \tag{B4}$$

Equation (B4) shows the repulsion of two eigenfrequencies when $\alpha > 0$ and gives rise to two EPs when $\alpha < 0$.

APPENDIX C: DIABOLIC POINT FOR SMALL INTERPAIR COUPLINGS

Physically, this case means the interpair coupling is much smaller than interpair frequency difference, i.e., $(2|t|/\Delta\omega) \ll 1$, so we could expand t in Eq. (A4) to leading order:

$$\begin{aligned} H \approx &\begin{pmatrix} \omega_2 - |\kappa| - i\frac{\Gamma+\Gamma_0}{2} & -i\frac{\Delta\Gamma}{2} & 0 & 0 \\ -i\frac{\Delta\Gamma}{2} & \omega_2 + |\kappa| - i\frac{\Gamma+\Gamma_0}{2} & 0 & 0 \\ 0 & 0 & \omega_1 - |\kappa| - i\frac{\Gamma+\Gamma_0}{2} & i\frac{\Delta\Gamma}{2} \\ 0 & 0 & i\frac{\Delta\Gamma}{2} & \omega_1 + |\kappa| - i\frac{\Gamma+\Gamma_0}{2} \end{pmatrix} \\ &+ \left(\frac{|t|}{\Delta\omega}\right)\overleftrightarrow{I}\begin{pmatrix} 0 & 0 & 0 & -i\Delta\Gamma \\ 0 & 0 & -i\Delta\Gamma & 0 \\ 0 & -i\Delta\Gamma & 0 & 0 \\ -i\Delta\Gamma & 0 & 0 & 0 \end{pmatrix}. \end{aligned} \tag{C1}$$

It is not difficult to see from Eq. (C1) that if $t = 0$, two pairs become decoupled, so we can write down eigenfrequencies from Eq. (A5):

$$\tilde{\omega}_j = \omega_0 - i\frac{\Gamma + \Gamma_0}{2} \pm \frac{1}{2}\left(\Delta\omega \pm \sqrt{4\kappa^2 - \Delta\Gamma^2}\right). \quad \text{(C2)}$$

Eigenstates 2 and 3 could cross over each other at particular $\Delta\Gamma$ as

$$\Delta\Gamma \equiv \Gamma_d = \sqrt{4\kappa^2 - (\Delta\omega)^2}. \quad \text{(C3)}$$

Such a crossover exists when $(\Delta\omega)^2 < 4\kappa^2$, which means intrapair coupling is strong enough to create a mode inversion. Under such conditions, we expand Eq. (C1) using $\Delta\Gamma = \Gamma_d + \delta\Gamma$ to the first order in $\delta\Gamma$ and t, and then find a reduced 2×2 Hamilton for states 2 and 3:

$$\begin{aligned} H_{\text{red}} &= \left[\omega_0 - \frac{i}{2}(2\Gamma_0 + \Gamma_d + \delta\Gamma)\right]\overleftrightarrow{I} \\ &\quad + \left(\frac{\Gamma_d}{2\Delta\omega}\right)\overleftrightarrow{I}\begin{pmatrix} \delta\Gamma & i2|t| \\ i2|t| & -\delta\Gamma \end{pmatrix} \\ &= \left[\omega_0 - \frac{i}{2}(2\Gamma_0 + \Gamma_d + \delta\Gamma)\right]\overleftrightarrow{I} \\ &\quad + \left(\frac{\Gamma_d}{2\Delta\omega}\right)\overleftrightarrow{I}(\delta\Gamma\sigma_z + i2|t|\sigma_x), \end{aligned} \quad \text{(C4)}$$

where σ_z and σ_x are Pauli matrices. The kernel in the second bracket determines the bifurcation. We can rotate spin space and rewrite the kernel as

$$H_{\text{eff}} = -\delta\Gamma\sigma_x + i2|t|\sigma_z, \quad \text{(C5)}$$

from which it is easy to see that interpair coupling t plays the role of an "imaginary mass." From Eqs. (C4) and (C5), we find the eigenfrequencies as

$$\tilde{\omega}_{2,3} = \omega_0 - \frac{i}{2}(2\Gamma_0 + \Gamma_d + \delta\Gamma) \pm \left(\frac{\Gamma_d}{2\Delta\omega}\right)\sqrt{(\delta\Gamma)^2 - 4t^2}. \quad \text{(C6)}$$

The corresponding eigenvectors are

$$\vec{a}_\pm = \begin{pmatrix} i\left(-\frac{\delta\Gamma}{2|t|} \mp \sqrt{\left(\frac{\delta\Gamma}{2t}\right)^2 - 1}\right) \\ 1 \end{pmatrix}. \quad \text{(C7)}$$

Thus, two EPs occur when $\delta\Gamma = \pm 2|t|$ and the two opposite signs correspond to a pair of EPs with opposite chiralities. The coalescence of such a pair forms a diabolic point, as shown in Fig. 5.

[1] W. Heiss, *The Physics of Exceptional Points*, J. Phys. A **45**, 444016 (2012).

[2] I. Rotter, *A Non-Hermitian Hamilton Operator and the Physics of Open Quantum Systems*, J. Phys. A **42**, 153001 (2009).

[3] H. Eleuch and I. Rotter, *Open Quantum Systems and Dicke Superradiance*, Eur. Phys. J. D **68**, 74 (2014).

[4] C. M. Bender and S. Boettcher, *Real Spectra in Non-Hermitian Hamiltonians Having PT Symmetry*, Phys. Rev. Lett. **80**, 5243 (1998); C. M. Bender, D. C. Brody, and H. F. Jones, *Complex Extension of Quantum Mechanics*, Phys. Rev. Lett. **89**, 270401 (2002).

[5] S.-Y. Lee, J.-W. Ryu, J.-B. Shim, S.-B. Lee, S. W. Kim, and K. An, *Divergent Petermann Factor of Interacting Resonances in a Stadium-Shaped Microcavity*, Phys. Rev. A **78**, 015805 (2008).

[6] A. M. van der Lee, N. J. van Druten, A. L. Mieremet, M. A. van Eijkelenborg, Å. M. Lindberg, M. P. van Exter, and J. P. Woerdman, *Excess Quantum Noise due to Nonorthogonal Polarization Modes*, Phys. Rev. Lett. **79**, 4357 (1997).

[7] B. Peng, Ş. K. Ozdemir, S. Rotter, H. Yilmaz, M. Liertzer, F. Monifi, C. M. Bender, F. Nori, and L. Yang, *Loss-Induced Suppression and Revival of Lasing*, Science **346**, 328 (2014).

[8] H. Hodaei, M.-A. Miri, M. Heinrich, D. N. Christodoulides, and M. Khajavikhan, *Parity-Time–Symmetric Microring Lasers*, Science **346**, 975 (2014).

[9] L. Feng, Z. J. Wong, R.-M. Ma, Y. Wang, and X. Zhang, *Single-Mode Laser by Parity-Time Symmetry Breaking*, Science **346**, 972 (2014).

[10] M. Brandstetter, M. Liertzer, C. Deutsch, P. Klang, J. Schöberl, H. E. Türeci, G. Strasser, K. Unterrainer, and S. Rotter, *Reversing the Pump Dependence of a Laser at an Exceptional Point*, Nat. Commun. **5**, 4034 (2014).

[11] S. Longhi, *Bloch Oscillations in Complex Crystals with PT Symmetry*, Phys. Rev. Lett. **103**, 123601 (2009).

[12] Y. Sun, W. Tan, H. Q. Li, J. Li, and H. Chen, *Experimental Demonstration of a Coherent Perfect Absorber with PT Phase Transition*, Phys. Rev. Lett. **112**, 143903 (2014).

[13] L. Chang, X. Jiang, S. Hua, C. Yang, J. Wen, L. Jiang, G. Li, G. Wang, and M. Xiao, *Parity-Time Symmetry and Variable Optical Isolation in Active-Passive-Coupled Microresonators*, Nat. Photonics **8**, 524 (2014).

[14] A. Guo, G. J. Salamo, D. Duchesne, R. Morandotti, M. Volatier-Ravat, V. Aimez, G. A. Siviloglou, and D. N. Christodoulides, *Observation of PT-Symmetry Breaking in Complex Optical Potentials*, Phys. Rev. Lett. **103**, 093902 (2009).

[15] Z. Lin, H. Ramezani, T. Eichelkraut, T. Kottos, H. Cao, and D. N. Christodoulides, *Unidirectional Invisibility Induced by PT-Symmetric Periodic Structures*, Phys. Rev. Lett. **106**, 213901 (2011).

[16] L. Feng, Y.-L. Xu, W. S. Fegadolli, M.-H. Lu, J. E. B. Oliveira, V. R. Almeida, Y.-F. Chen, and A. Scherer, *Experimental Demonstration of a Unidirectional Reflectionless Parity-Time Metamaterial at Optical Frequencies*, Nat. Mater. **12**, 108 (2012).

[17] B. Peng, Ş. K. Özdemir, F. Lei, F. Monifi, M. Gianfreda, G. L. Long, S. Fan, F. Nori, C. M. Bender, and L. Yang, *Parity-Time-Symmetric Whispering-Gallery Microcavities*, Nat. Phys. **10**, 394 (2014).

[18] C. E. Rüter, K. G. Makris, R. El-Ganainy, D. N. Christodoulides, M. Segev, and D. Kip, *Observation of Parity–Time Symmetry in Optics*, Nat. Phys. **6**, 192 (2010).
[19] Y. D. Chong, L. Ge, and A. D. Stone, *PT-Symmetry Breaking and Laser-Absorber Modes in Optical Scattering Systems*, Phys. Rev. Lett. **106**, 093902 (2011).
[20] A. Regensburger, C. Bersch, M.-A. Miri, G. Onishchukov, D. N. Christodoulides, and U. Peschel, *Parity-Time Synthetic Photonic Lattices*, Nature (London) **488**, 167 (2012).
[21] K. G. Makris, R. El-Ganainy, D. N. Christodoulides, and Z. H. Musslimani, *Beam Dynamics in PT Symmetric Optical Lattices*, Phys. Rev. Lett. **100**, 103904 (2008).
[22] R. Fleury, D. L. Sounas, and A. Alù, *An Invisible Acoustic Sensor Based on Parity-Time Symmetry*, Nat. Commun. **6**, 5905 (2015).
[23] X. F. Zhu, H. Ramezani, C. Z. Shi, J. Zhu, and X. Zhang, *PT-Symmetric Acoustics*, Phys. Rev. X **4**, 031042 (2014).
[24] C. Dembowski, H.-D. Gräf, H. L. Harney, A. Heine, W. D. Heiss, H. Rehfeld, and A. Richter, *Experimental Observation of the Topological Structure of Exceptional Points*, Phys. Rev. Lett. **86**, 787 (2001); C. Dembowski, B. Dietz, H.-D. Gräf, H. L. Harney, A. Heine, W. D. Heiss, and A. Richter, *Observation of a Chiral State in a Microwave Cavity*, Phys. Rev. Lett. **90**, 034101 (2003).
[25] T. Gao *et al.*, *Observation of Non-Hermitian Degeneracies in a Chaotic Exciton-Polariton Billiard*, Nature (London) **526**, 554 (2015).
[26] H. Cartarius and G. Wunner, *Model of a PT-Symmetric Bose-Einstein Condensate in a δ-Function Double-Well Potential*, Phys. Rev. A **86**, 013612 (2012).
[27] F. Single, H. Cartarius, G. Wunner, and J. Main, *Coupling Approach for the Realization of a PT-Symmetric Potential for a Bose-Einstein Condensate in a Double Well*, Phys. Rev. A **90**, 042123 (2014).
[28] P. San-Jose, J. Cayao, E. Prada, and R. Aguado, *Majorana Bound States from Exceptional Points in Non-Topological Superconductors*, Sci. Rep. **6**, 21427 (2016).
[29] B. Zhen, C. W. Hsu, Y. Igarashi, L. Lu, I. Kaminer, A. Pick, S.-L. Chua, J. D. Joannopoulos, and M. Soljačić, *Spawning Rings of Exceptional Points Out of Dirac Cones*, Nature (London) **525**, 354 (2015).
[30] N. X. A. Rivolta and B. Maes, *Symmetry Recovery for Coupled Photonic Modes with Transversal PT Symmetry*, Opt. Lett. **40**, 3922 (2015).
[31] H. Benisty, A. Lupu, and A. Degiron, *Transverse Periodic PT Symmetry for Modal Demultiplexing in Optical Waveguides*, Phys. Rev. A **91**, 053825 (2015).
[32] K. Ding, Z. Q. Zhang, and C. T. Chan, *Coalescence of Exceptional Points and Phase Diagrams for One-Dimensional PT Symmetric Photonic Crystals*, Phys. Rev. B **92**, 235310 (2015).
[33] W. Heiss, *Chirality of Wavefunctions for Three Coalescing Levels*, J. Phys. A **41**, 244010 (2008).
[34] G. Demange and E.-M. Graefe, *Signatures of Three Coalescing Eigenfunctions*, J. Phys. A **45**, 025303 (2012).
[35] S.-Y. Lee, J.-W. Ryu, S. W. Kim, and Y. Chung, *Geometric Phase around Multiple Exceptional Points*, Phys. Rev. A **85**, 064103 (2012).
[36] G. Levai, F. Ruzicka, and M. Znojil, *Three Solvable Matrix Models of a Quantum Catastrophe*, Int. J. Theor. Phys. **53**, 2875 (2014).
[37] M. V. Berry and M. Wilkinson, *Diabolical Points in the Spectra of Triangles*, Proc. R. Soc. A **392**, 15 (1984).
[38] See Supplemental Material at http://link.aps.org/supplemental/10.1103/PhysRevX.6.021007 for analysis of experimental uncertainties and theoretical details about different classes in the phase diagram.
[39] W. D. Heiss and G. Wunner, *Resonance Scattering at Third-Order Exceptional Points*, J. Phys. A **48**, 345203 (2015).
[40] A. A. Soluyanov and D. Vanderbilt, *Smooth Gauge for Topological Insulators*, Phys. Rev. B **85**, 115415 (2012).